

## Research Article

# Research on the Mechanical Characteristics of Cyclic Loading and Unloading of Rock Based on Infrared Thermal Image Analysis

Lewen Wu,<sup>1,2</sup> Keping Zhou,<sup>1,2</sup> Feng Gao,<sup>1,2</sup> Zhongyuan Gu,<sup>1,2</sup> and Chun Yang<sup>1,2</sup> 

<sup>1</sup>School of Resources and Safety Engineering, Central South University, Changsha 410083, Hunan, China

<sup>2</sup>Research Center for Mining Engineering and Technology in Cold Regions, Central South University, Changsha 410083, Hunan, China

Correspondence should be addressed to Chun Yang; [chunyang@csu.edu.cn](mailto:chunyang@csu.edu.cn)

Received 20 February 2021; Revised 22 March 2021; Accepted 26 March 2021; Published 12 April 2021

Academic Editor: Zhigang Tao

Copyright © 2021 Lewen Wu et al. This is an open access article distributed under the Creative Commons Attribution License, which permits unrestricted use, distribution, and reproduction in any medium, provided the original work is properly cited.

In the operations of underground rock engineering, such as mining, the formation of goafs is often accompanied by unloading and energy effects. In this study, a cyclic loading and unloading stress test is carried out to analyze the strength characteristics of the loaded samples under different loading and unloading ranges as well as different numbers of cycles. The rock force is accompanied by substantial energy changes. To better fit the energy analysis under cyclic loading and unloading conditions, thermal infrared radiation characteristic analysis is performed during rock loading and unloading. An infrared radiation camera is adopted to detect the infrared characteristics of the rock force process after cyclic loading and unloading. Multiangle detection is implemented on the temperature, temperature field, and frequency histogram. The analysis shows that cyclic loading and unloading first strengthen and then weaken the rock. Moreover, the failure caused by the local stress concentration leads to a sharp increase in the temperature. There are significant temperature fluctuations before and after failure, and the temperature field after failure can be divided into three zones, namely, the normal temperature zone, heating zone, and mutational temperature zone, to comprehensively reflect that rock compression failure which is accompanied by the process of energy accumulation and release. On the basis of infrared energy analysis, the index of the energy release rate is introduced, and the loading and unloading analysis model is constructed. The research results reveal that rock failure is accompanied by the process of energy accumulation and release, which provides evidence for the analysis of the spatial stability of the rock mass under cyclic loading and unloading conditions and engineering excavation.

## 1. Introduction

As the foundation of industrial development, the mining industry not only promotes the development of social history and the progress of human civilization but also makes a substantial contribution to a country's economic development and national defense [1–3]. The development of the traditional mining industry is costly to the ecological environment. Especially in the last century, the phenomena of random mining and digging, overexploiting rich mines, and abandoning poor mines have become even worse [4–8]. A large number of goafs and substantial waste rocks, residues, tailings, etc., not only cause serious safety issues, such as reservoir dam failure, goaf collapse, waste rock landslides, and groundwater pollution but also severely destroy the

natural environment [9, 10]. Despite early-stage low-level mining or various high-efficiency open-field mining techniques, numerous goafs will be formed during the mining process. If they appear in groups and fail to be dealt with in time, the possibility of inducing collapse will greatly increase [11–14]. In actual engineering applications, most goaf disasters occur from slow deformation to sudden collapse. It should also be noted that the underground goaf groups are open, complex, and nonlinear. Therefore, both their formation and the mining of their adjacent ore bodies involve the development of fissures in the surrounding rock under the mechanical action of rock loading and unloading [15, 16]. If these factors are ignored, it will inevitably lead to unexpected disasters in the goaf, which will not only miss the appropriate disposal opportunity but will also pose a serious

security threat to later mining and recovery of residual mineral resources.

Although many scholars have long recognized that the unloading analysis method is more suitable for the excavation of underground rock mass engineering than the loading analysis method, so far, there is no established unloading analysis method. In addition, in underground mining, because the mining process is composed of multiple repeated blasts, coupled with the influence of adjacent stopes, the surrounding rock is actually in a state of repeated loading and unloading [17]. After this state is over, the mechanical properties of the rock mass are actually the properties after cyclic loading and unloading, which is difficult to reflect in the current analysis methods.

It is acknowledged that the mechanical properties of the rock under unloading are closer to the response characteristics of the surrounding rock in actual underground engineering excavation. Many researches have been conducted numerically or experimentally to study the rock behavior under unloading condition [18]. Yang et al. performed numerical investigation on roof with the approach of instantaneous unloading, which given a reasonable guidance in mining practice [19]. Sun et al. and Yang et al. used a numerical approach to study the rock failure behavior under unloading conditions [20, 21]. Meng et al. and Li et al. conducted experimental tests of rock under the conditions of cyclic loading and unloading [22, 23]. Zhou et al. studied the rock damage evolution characteristics of unloading rock with nuclear magnetic resonance tests [24]. Chen et al. experimentally studied the crack propagation behaviors of rock by considering different confining pressure levels [25].

The excavation of underground rock masses is a typical unloading process that has been recognized by a large number of scholars, but the current conventional analysis angle still requires a deeper understanding. Observing and studying rock mechanics problems from the perspective of energy have attracted increasing attention from engineering and theoretical circles [26–28]. With the advancement of technology, there are an increasing number of methods for exploring the internal fractures of rocks, and the accuracy is increasing. Bazaikin et al. [29–33] applied real-time scanning technology to study the internal microcrack propagation of geotechnical materials and explored the law of failure changes through numerical changes. Lin et al. [34] combined energy theory and the discrete element method to analyze the mechanical characteristics of double-circular-hole jointed rock masses under uniaxial loading and studied the influence of different joint parameters on the strength and failure behavior of double-circular-hole jointed rock masses. Cao et al. [35] simulated and analyzed the microscale fracturing and energy transfer process of transversely isotropic rocks with different dip angles based on the plane joint contact model in the particle flow method. Rasmussen et al. [36] adopted the Monte Carlo simulation method of cloud computing technology to complete the 3D probabilistic stability analysis of a tunnel using the energy evolution of the unsupported section of the shallow rock tunnel. In the final analysis, the failure of rock is a phenomenon of state

instability driven by energy. The study of energy transfer and transformation in the process of rock deformation and failure can precisely reflect the law of rock failure. Therefore, studying the change law of the mechanical properties, the damage development law and the energy evolution law of rock under loading and unloading conditions, revealing the inter-relationship between the three, and carrying out unloading mechanical analyses based on multiangle tests and targeted energy analysis to more truly reflect the influence process and safety of underground engineering disturbances are of great theoretical significance and engineering value for the stability analysis, disposal, and subsequent recycling of residual mineral resources in underground goafs.

Laboratory tests are an effective approach to observe the mechanical behavior of rock under loading or unloading conditions [37, 38]. To observe the variation in the deformation, energy, or temperature during experiment tests on rocks, some advanced nondestructive measurement devices have been developed, such as infrared thermography, the use of high-speed cameras, and the digital image correlation method [39–41]. Among them, infrared thermography, which has recently been used to monitor surface temperature changes in rock experiments, was first developed for the military [42]. Therefore, the energy evolution during loading and unloading tests can be demonstrated by the infrared temperature change of the rock surface.

In response to these problems, this research takes the unloading rock mass of underground mine engineering as the object. Based on the theory of unloading mechanics, constant range loading and unloading and incremental loading and unloading methods are employed to carry out cyclic loading and unloading tests on rock samples. Taking into account the actual situation of the project, the number of cycles is generally set to five or ten, and the unloading ranges are 12%, 24%, 36%, 48%, and 60% of the strength of the rock sample, respectively, to analyze the deformation law of the rock during the test. According to the infrared imaging test method, the temperature field change law of the rock sample during the cyclic loading and unloading test is observed, and the mechanical state of the rock mass during the underground mining process, as well as the change law of the mechanical properties of the rock mass, are analyzed. In addition, the rock damage mechanics theory is combined to derive the internal energy density change function of the rock and reveal the law of energy migration and release of the rock mass under cyclic loading and unloading conditions, which provide a basis for underground geotechnical engineering construction and disturbance control.

## 2. Materials and Methods

*2.1. Materials and Devices.* The surrounding rock of the mine selected in this test is mainly granite qualified with high strength, excellent bearing performance, and favorable energy accumulation capacity. After cutting, drilling, and grinding the retrieved granite, it is processed into a cylindrical sample with a height of 100 mm and a diameter of 50 mm according to the height to diameter ratio of 2 : 1, and

the unevenness of the end surface is controlled to within 0.02 mm, which is in accordance with the Chinese standard GB/T 23561.7-2009.

A WDW-2000 servo stress testing machine is employed to carry out cyclic loading and unloading pretreatment and compression tests on rock. The infrared imager of the FLIR SC7300 system is used for infrared thermal imaging analysis. The instrument has strong adaptability, is small in size, and can simultaneously capture instantaneous images. It can realize an efficient connection between the FLIR SC7300 system and computer through plug and play interface, Camlink, or GigE interface.

## 2.2. Test Methods

*2.2.1. Mechanical Tests on Rock under Cyclic Loading and Unloading.* In this study, the uniaxial cyclic loading and unloading test is carried out on the basis of the rock uniaxial compression test. The test steps are as follows:

(1) Select the rock samples:

Since the test involves the comparative analysis of data from multiple tests before and after the tests are performed, it is preferable to select samples with uniform particles and similar densities as the analysis samples.

(2) Uniaxial compression test:

The samples for the uniaxial compression failure test were selected to obtain the uniaxial compressive strength and stress-strain curve of the rock.

(3) Cyclic loading and unloading test:

A uniaxial compression test is carried out on the rock samples of Group A to load the rock samples at one time, and the infrared signals generated during the deformation and failure of the rock under compression are simultaneously collected. The cyclic loading and unloading method is based on the peak value of the maximum uniaxial compressive strength, and the cyclic loading method for the remaining rock samples is to load the rock specimen to a certain proportion of the peak uniaxial maximum compressive strength and then unload it. The loading speed is 0.5 kN/s. Subsequently, according to the uniaxial compressive strength of the sample obtained by the rock uniaxial compression test, the test is divided into five groups according to the load of 12%, 24%, 36%, 48%, and 60% of the peak strength. Five and ten cycles of loading and unloading are performed, respectively, and then a uniaxial compression test is carried out on the samples to obtain the real-time uniaxial compressive strength and stress-strain curve.

In the abovementioned test, to ensure that the data are comparable, samples with more uniform particles are selected, and each group includes five samples. After the test, the samples with the maximum and minimum strength are removed, and the data of the middle three relatively average samples are analyzed.

*2.2.2. Infrared Radiation Energy Test.* The test is followed by the rock loading and unloading mechanical test, and the

infrared test is mainly performed during the uniaxial compression test on the rock that has finished loading and unloading. The test equipment is an infrared imager with a FLIR SC7300 system. When installing infrared detection equipment, it is required to control the detection distance at one meter and to control the temperature, noise, and light of the detection room. It is also necessary to use heat-insulating gloves when in contact with the sample.

The infrared data and image information are also observed during the test. The average infrared radiation temperature (AIRT) of the rock surface reflects the infrared radiation energy of the entire rock sample and is an important indicator for characterizing the changes in infrared radiation during the rock loading process [43–45]. Since the overall surface of the rock alternates frequently with the outside during the cyclic loading process, the contact between the end face of the rock and the press will affect the temperature field, and the internal energy accumulation of the rock will not easily exchange heat with the external environment, and the overall temperature field data (Area 1) of the sample and the temperature field data of the central location (Area 2) are tested separately. Area 1 is the average infrared radiation temperature of the lateral projection area (50 mm × 100 mm) of the overall rock sample, while Area 2 is a selected small area near the center (40 mm × 40 mm).

During the test, the samples that were subjected to the cyclic loading and unloading test were pretreated first, cooled to ambient temperature, and protected. Uniaxial compressive strength tests and simultaneous infrared tests were performed on the sample after pretreatment. After the test, the strength, AIRT, thermal imaging, and frequency histogram results were analyzed. A schematic diagram of the infrared test system is shown in Figure 1, and the test process is shown in Figure 2.

## 3. Analysis and Discussion

### *3.1. Mechanical Action of Rock Cyclic Loading and Unloading.*

According to the stress-strain relationship of the rock, combined with other related tests, the basic physical and mechanical parameters of this sample can be obtained, as shown in Table 1.

The cyclic unloading test results include the uniaxial compressive strength and elastic modulus of the sample after cyclic unloading. The uniaxial compression stress-strain curve of the granite sample in Table 2 shows that in Groups B and C, where the unloading and loading ranges are 12% and 24% of the uniaxial compressive strength, the loading and unloading values fall within the range of the microfracture compaction stage; in Groups D, E, and F, where the unloading and loading ranges are 36%, 48%, and 60% of the uniaxial compressive strength, the loading and unloading values fall within the range of the elastic deformation stage. When the range is 72%, it is difficult to achieve cyclic loading and unloading, which, therefore, has not been taken into consideration.

Table 2 suggests that the compressive strength of the rock samples will change after cyclic unloading, and the relevant

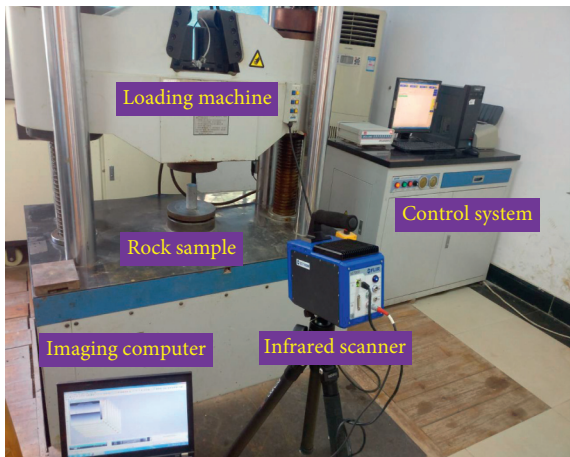
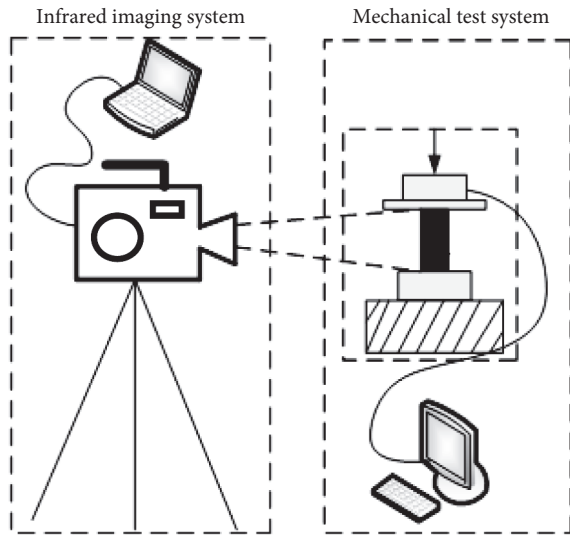


FIGURE 1: Configuration of experimental setup.

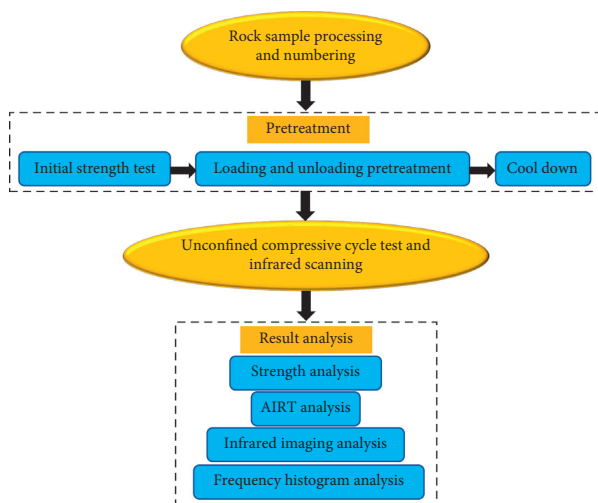


FIGURE 2: Flow chart of the infrared test.

change rules will be analyzed in the follow-up. The loading and unloading test curves of some samples are recorded, as shown in Figure 3.

After loading and unloading cycles of different intensities, the whole process of the uniaxial compression experiment is repeated on the sample, and the overall shape of the obtained stress-strain curve is basically similar to that of the initial sample. They both exhibit a high peak stress, and the microfracture compaction stage and elastic deformation stage are remarkable, and the postpeak stress drop is rapid, which shows that cyclic loading and unloading do not change the overall mechanical properties of the rock, which is consistent with the existing conclusions. To further analyze the mechanical properties of the rock under the action of cyclic loading and unloading and to provide a basis for the follow-up damage and failure mechanism discussion, a brief description of the morphology of typical samples after failure is provided.

Figure 4 shows the failure modes of rock samples after five cycles under different loading and unloading ranges. It can be seen from the figure that the failure mode of the sample is mainly shear failure and splitting failure. The sample that is not initially affected by cyclic loading and unloading (such as A-2) has a relatively complete failure surface that penetrates the sample when it fails, the failure is mainly due to fracture and damage along the surface, and the rock strength is high. When the unloading range is low, the internal pores of the rock do not change significantly, the failure surface remains relatively complete, and the rock strength is also high; as the loading and unloading range increases, the number and volume of pores inside the rock will also grow, which will intensify the internal damage of the rock. In the meantime, the sample will show “X” type shear failure, and the shear surface generally penetrates the entire sample. There are varying amounts of small local rock caving, and the greater the loading and unloading range is, the fewer the large blocks there are, the more the broken blocks there are, and the more uniform the block size after failure is.

Figure 5 demonstrates the failure modes of rock samples after ten cycles under different loading and unloading ranges. The figure states that the damage mode of the sample is the same overall damage mode as that under five cycles, but the damage is more thorough. Under the loading and unloading range of 12%, the internal flaws (pores, microcracks, etc.) of the rock are indeed reduced. It appears as sample B-21, which is damaged along a very complete failure surface, and there are few other fragments. At this moment, the rock strength increases slightly. Compared with Figure 4, due to the increase in the number of loading and unloading cycles, as the loading and unloading range increases, the internal damage of the rock also rises; that is, the more the pores and volume there are, the greater the degree of rock damage, and the smaller the uniform fragments. Especially when the loading and

TABLE 1: Basic physical and mechanical parameters of the rock samples.

Sample no.	Density (kg/m <sup>3</sup> )	Uniaxial compressive strength (MPa)	Elastic modulus (GPa)
A-1	2710	190.5	73.56
A-2	2710	193.2	75.54
A-3	2700	196.4	77.84

TABLE 2: Cycle test scheme and related results.

Sample no.	Cycles	Loading and unloading range ratio (%)	Uniaxial compressive strength (MPa)	Elastic modulus (GPa)
B-11	5	12	190.4	74.7
B-12	5	12	189.4	74.31
B-13	5	12	195.3	76.32
B-21	10	12	195.3	78.8
B-22	10	12	194.7	78.61
B-23	10	12	193.6	75.43
C-11	5	24	183.4	73.15
C-12	5	24	185.7	77.84
C-13	5	24	187.6	75.36
C-21	10	24	180.8	67.69
C-22	10	24	180.9	69.07
C-23	10	24	185.3	69.87
D-11	5	36	177.0	63.95
D-12	5	36	175.2	61.25
D-13	5	36	179.6	67.27
D-21	10	36	174.8	62.45
D-22	10	36	173.9	62.84
D-23	10	36	171.3	61.89
E-11	5	48	164.8	62.04
E-12	5	48	160.2	60.32
E-13	5	48	167.9	58.64
E-21	10	48	163.4	57.23
E-22	10	48	154.6	53.41
E-23	10	48	159.9	55.5
F-11	5	60	156.7	50.36
F-12	5	60	152.2	51.02
F-13	5	60	155.3	59.11
F-21	10	60	144.9	54.31
F-22	10	60	153.1	49.36
F-23	10	60	140.5	47.25

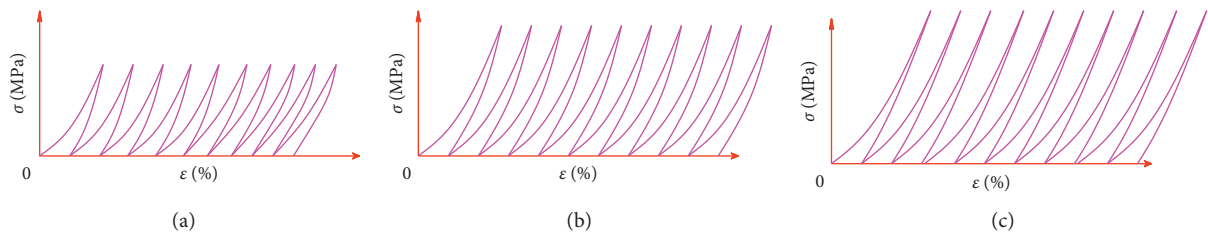


FIGURE 3: Stress-strain curves of typical samples. (a) Range 12%, cycles 10, and sample B-21. (b) Range 36%, cycles 10, and sample D-21. (c) Range 60%, cycles 10, and sample F-21.

unloading cycle range reaches 60%, sample F-21 shows a uniform and fine distribution of fragments after failure, and a large amount of powdery debris is generated, which indicates that not only the internal damage of the rock increases, but the internal pores are also uniformly distributed.

**3.1.1. Strength Analysis.** For most samples, the overall change trend of the uniaxial compressive strength of the rock decreases with increasing loading and unloading range and number of cycles. This influence comes from both the loading and unloading range and the number of loading and

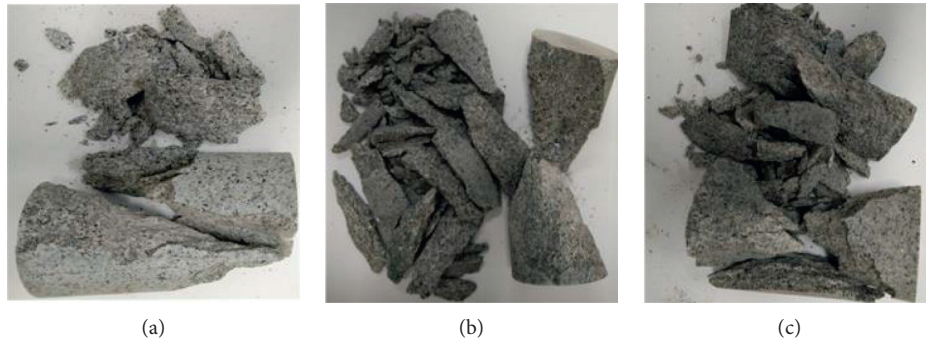


FIGURE 4: Pictures of rock sample failure for different loading and unloading ranges under five cycles. (a) A-2. (b) C-12. (c) E-11.

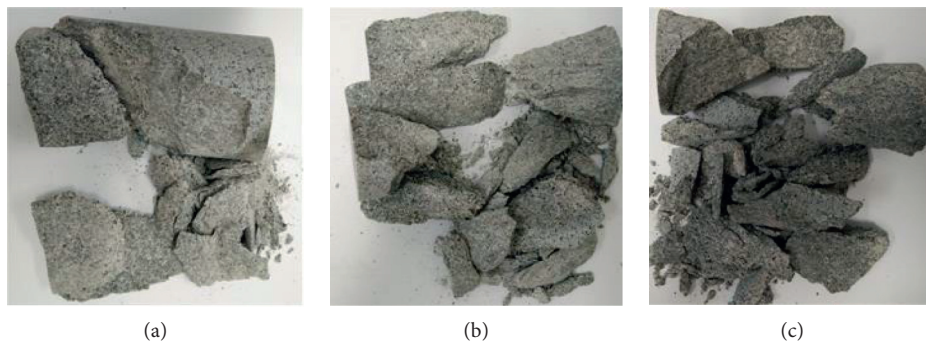


FIGURE 5: Pictures of rock sample failure under ten cycles of different loading and unloading ranges. (a) B-21. (b) D-22. (c) F-21.

unloading cycles; therefore, it needs to be analyzed separately. As shown in Figure 6, the uniaxial compressive strength of rock under different loading and unloading ranges has the following characteristics:

- (i) With the increase in the loading and unloading range, the uniaxial compressive strength of the rock gradually decreases. The average uniaxial compressive strength of the initial sample, that is, the sample that has not undergone loading and unloading, is approximately 193.4 MPa. After five cycles of loading and unloading, the average compressive strength of the samples with different loading and unloading ranges changes to 191.7 MPa, 177.3 MPa, 164.3 MPa, and 154.7 MPa. Similarly, after 10 loading and unloading cycles, the average compressive strength of the samples with different loading and unloading ranges becomes 195.5 MPa, 181.2 MPa, 173.3 MPa, 159.3 MPa, and 146.2 MPa, and the decreasing trend is rather obvious.
- (ii) When the loading and unloading range is in the stage of microfracture compaction, the uniaxial compressive strength of the rock remains almost unchanged. Regardless of five or ten loading and unloading cycles, the uniaxial compressive strength of the rock remains almost unchanged at the loading and unloading range of 12% and even slightly increases under the condition of ten loading and unloading cycles. When the loading and unloading range is small, the inside of the rock is mainly

compacted by microcracks, which has little effect on the mechanical properties of the rock. The possible reason why the strength increases slightly after ten loading and unloading cycles is that continuous loading and unloading compact some of the smaller cracks in the rock that cannot be compacted under normal conditions, limiting the crack propagation of the rock sample to a certain extent in the follow-up force phase.

- (iii) As the range of loading and unloading increases, the rate of decrease in the compressive strength of rock is also magnified. After five loading and unloading cycles, the uniaxial compressive strength differences between different loading and unloading ranges are 1.7 MPa, 6.1 MPa, 8.3 MPa, 13 MPa, and 9.6 MPa. This shows that during the loading and unloading process, when the loading and unloading value approaches or even exceeds the elastic limit of the sample, irreversible damage will occur inside the rock, which will lead to obvious cracks in the sample after cyclic loading and unloading. Therefore, the greater the loading and unloading range is and the closer the range is to the elastic limit of the rock, the greater the reduction of rock strength.

*3.1.2. Elastic Modulus Analysis.* Similar to the change law of the uniaxial compressive strength, for most samples, the elastic modulus of rock decreases with the increase in the range of loading and unloading and the cycle index. Since

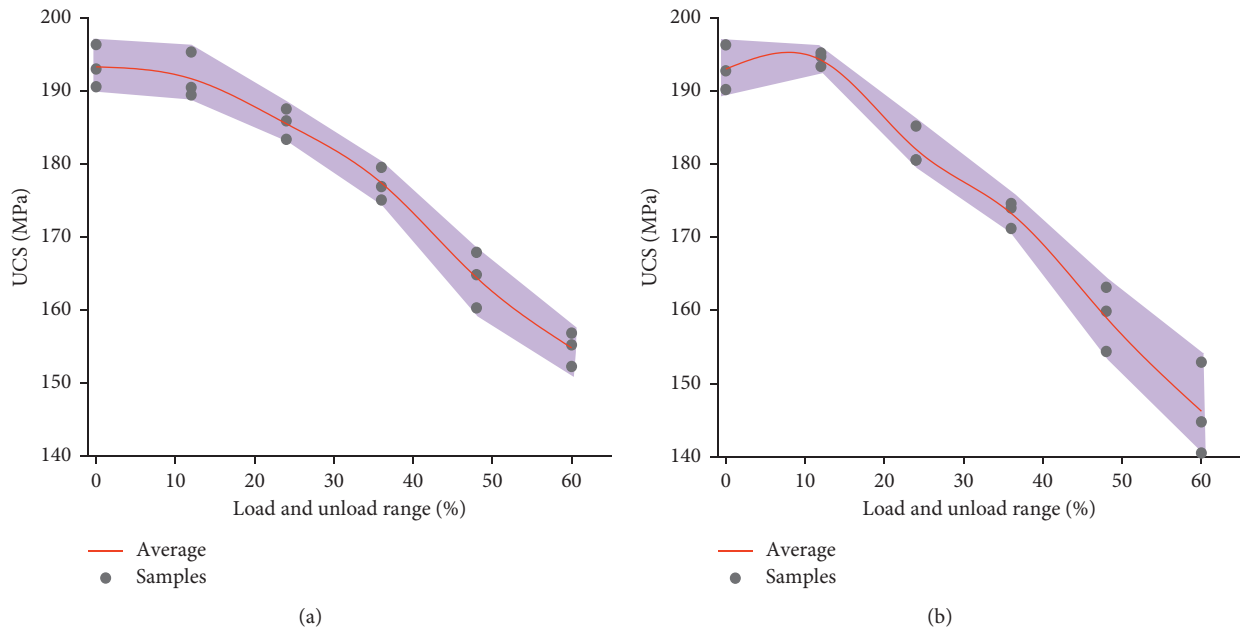


FIGURE 6: Variation curve of the uniaxial compressive strength of samples under different loading and unloading ranges. (a) Five cycles of loading and unloading. (b) Ten cycles of loading and unloading.

the elastic modulus is often considered a major indicator to measure rock quality and damage changes in rock mechanics, it should be analyzed. As shown in Figure 7, the change rule of the elastic modulus is also different from that of the uniaxial compressive strength. The characteristics of the elastic modulus of rock under different loading and unloading ranges are summarized as follows:

- (i) With increasing loading and unloading range, the elastic modulus of the rock gradually declines. The average elastic modulus of the samples before loading and unloading is approximately 75.65 GPa, which is within the range of the elastic modulus of ordinary granite. After five loading and unloading cycles, the average elastic modulus of the samples with different loading and unloading ranges became 75.11 GPa, 74.26 GPa, 64.12 GPa, 60.33 GPa, and 50.69. Similarly, after 10 cycles of loading and unloading, the values became 77.61 GPa, 64.21 GPa, 62.39 GPa, 55.38 GPa, and 50.31 GPa, and the decreasing trend was quite obvious.
- (ii) When the loading and unloading range is small, the elastic modulus of the rock remains almost unchanged. When the number of loading and unloading cycles is 5, the reduction in the elastic modulus of the rock is very limited at loading and unloading ranges of 12% and 24%, and the 24% loading and unloading range is near the starting point of the elastic deformation section of the sample. This shows that when loading and unloading occur in the early stage of the elastic deformation of rock, the cycle index is small, and the elastic modulus of rock is not substantially affected.
- (iii) When the number of loading and unloading cycles is small, with increasing loading and unloading

range, the rate of decrease in the elastic modulus also increases, which is quite different from the change in the uniaxial compressive strength. After five loading and unloading cycles, the average differences in the elastic modulus between different loading and unloading ranges are 0.53 GP, 0.86 GPa, 10.10 GPa, 3.83 GPa, and 9.64 GPa, where three stages are obviously formed. After 10 loading and unloading cycles, except for a slight increase at 12% of the loading and unloading range, the elastic moduli at other loading and unloading ranges are almost uniformly reduced.

*3.2. Thermodynamic Law of Rock Loading and Unloading Based on Infrared Tests.* After the pretreatment of each group of cyclically loaded and unloaded samples, they are placed on the ground and cooled to ambient temperature. The uniaxial compressive strength test is carried out under effective protection with infrared inspection conducted at the same time. The overall average infrared radiation temperatures of rock surface area 1 (50 mm × 100 mm side projection area) and central area 2 (near the center 40 mm × 40 mm area) are detected. It can be concluded that rock failure is accompanied by significant infrared radiation, and the average temperature of the central area is significantly higher than that of the overall rock. The infrared radiation temperature AIRT of the original rock sample is tested: Area 1 is 23.6°C, and Area 2 is 23.81°C. The AIRT test results during the uniaxial compression test on the rock under each cycle of loading and unloading are summarized, and the average temperature is calculated by testing applications. The results are shown in Table 3, and the result comparison curve is shown in Figure 8. The AIRT detection

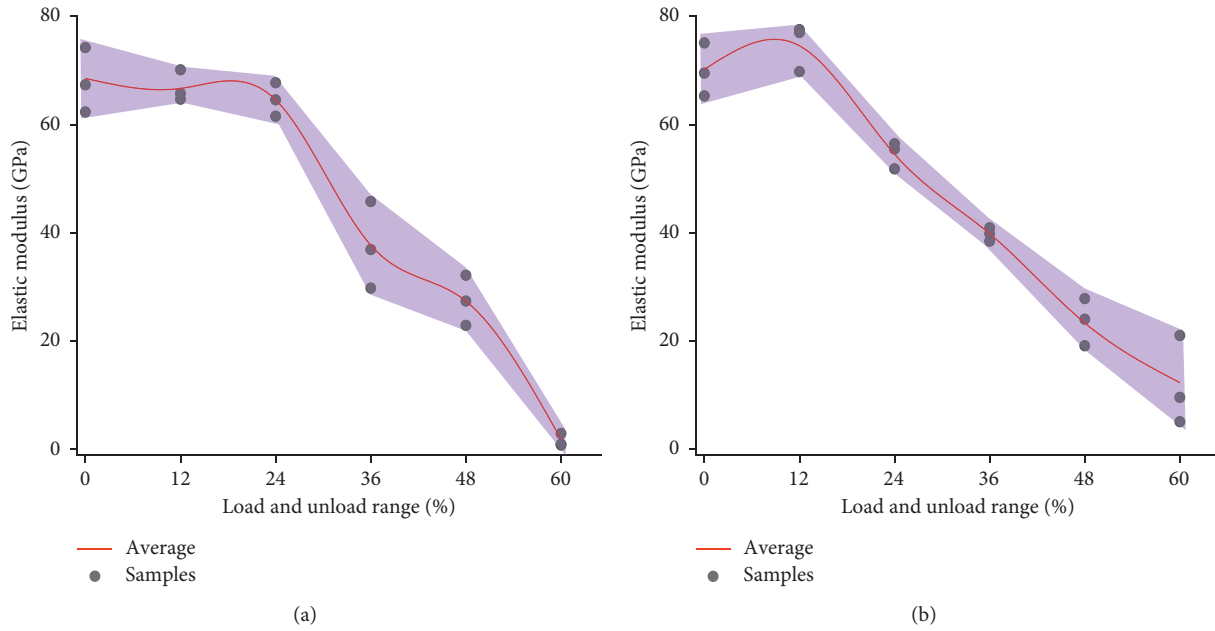


FIGURE 7: Variation curve of the elastic modulus of the sample under different loading and unloading ranges. (a) Five cycles of loading and unloading. (b) Ten cycles of loading and unloading.

TABLE 3: ATRT results.

Range (%)		12	24	36	48	60
Five cycles	Area 1 AIRT (°C)	23.59	24.08	24.16	24.26	24.66
	Area 2 AIRT (°C)	24.45	24.65	24.88	25	25.09
Ten cycles	Area 1 AIRT (°C)	23.91	24.56	24.59	24.58	23.71
	Area 2 AIRT (°C)	24.53	24.86	25.8	24.88	24.2

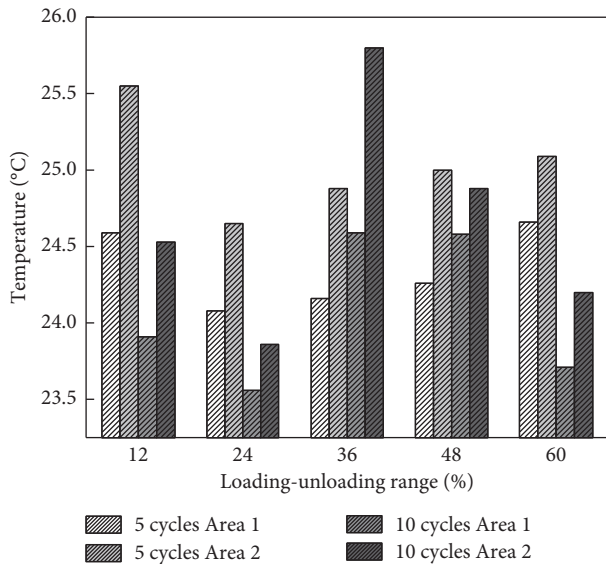


FIGURE 8: AIRT results.

diagram of the rock sample at the 60% range is selected as the representative schematic diagram, as shown in Figure 9.

Figure 8 suggests that the damage is less under five cycles, and the accumulated energy can play a better role in forming a more obvious thermal energy conversion, while

under ten cycles, the damage is correspondingly augmented. The smaller the loading and unloading range, the higher the temperature, and vice versa. The comparative strength test shows that there is a certain correlation between the strength and the infrared temperature performance. The temperature is higher under ten cycles with a range of 36%, which is consistent with the strength results.

As shown in Figure 9, the rock has no obvious temperature change before failure, and the temperature curve is stable, but it is accompanied by a significant temperature rise during failure. This states that significant energy exchange occurs during destruction, and heat release takes place. The average temperature in the central area is significantly higher than the overall average temperature, indicating that rock failure is a heating process, there is obvious heat exchange with the outside world, and the temperature in the central area is higher. The results of infrared scanning show that there are notable temperature fluctuations when the rock mass is broken, that is, the up and down fluctuations before the peak, the sharp rise when it is destroyed, and then the decline. In addition, the magnitude of the increase has a greater correlation with the average temperature of the detection. In conclusion, the rock failure process is accompanied by a substantial temperature field change, which can provide a rock failure evaluation platform from the perspective of energy.

To analyze the infrared characteristics of the rock at the moment of failure, infrared imaging detection and analysis of the failure process are performed, as shown in Figure 10. This demonstrates that rock failure will cause a nonuniform instantaneous temperature increase. The failure is stress concentration-induced failure in individual areas, which in turn leads to overall instability failure. The failure process is accompanied by substantial temperature differences. Before

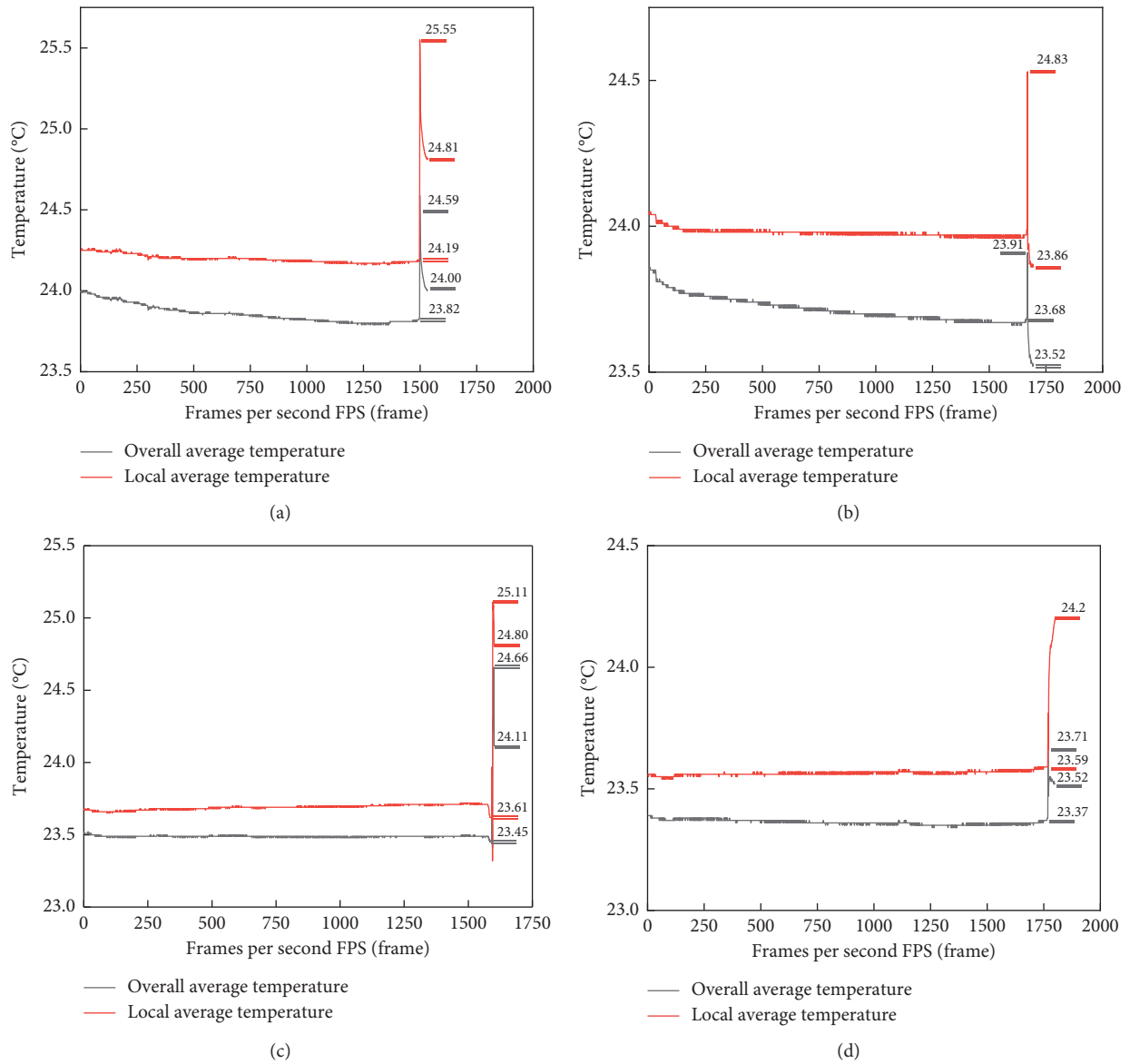


FIGURE 9: AIRT curve of the rock compression test under different loading and unloading ranges. (a) 12% range, five cycles, and sample B-11. (b) 12% range, ten cycles, and sample B-21. (c) 60% range, five cycles, and sample F-11. (d) 60% range, ten cycles, and sample F-21.

the destruction, there is almost no change. During destruction, a high-temperature area appears locally on the surface layer, and an internal high-temperature area appears after destruction. After destruction, the high-temperature area exchanges energy with the environment, and the temperature gradually drops. Comparing the failure states of different cycles, a conclusion can be drawn that multiple cycles will result in fatigue of the rock material and reduce its energy storage capacity. Rock failure after ten cycles will occur before the formation of a wide range of high temperatures. The stress concentration in some areas will cause damage first, and then the disaster area will penetrate, leading to overall damage. The high-temperature area is also consistent with the failure fracture pattern. Through infrared detection, the stress concentration, regional concentration, and distribution of the damaged exposed area can be

detected. Concurrently, with increasing range and number of cycles, the exposure to high-temperature points showed a decreasing trend. It is inferred that due to the increase in damage, the stress concentration in the rock decreases, and the damage becomes more uniform.

The frequency histogram can simplify the data and highlight the statistical distribution and structural characteristics of the data. Therefore, the frequency histogram is adopted to analyze the temperature distribution characteristics of the rock failure process. The frequency histograms of the representative rock samples with ranges of 48% and 60% after 10 cycles are shown in Figures 11 and 12, respectively. The frequency histograms reflect that the corresponding temperature with a high frequency is the regional center temperature, and the temperature range reflects the uniformity of the regional temperature field.

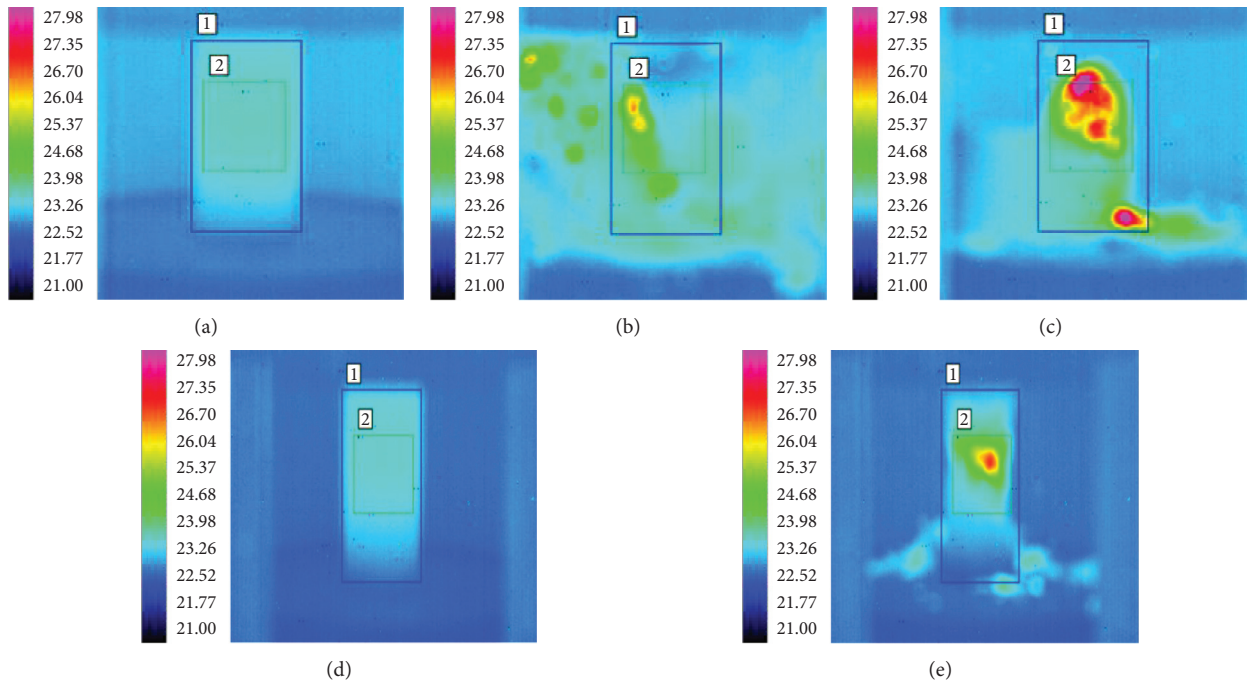


FIGURE 10: Thermal imaging of the unidirectional cyclic load at 60% of the range; Area 1: 50 mm × 100 mm; Area 2: 240 mm × 40 mm. (a) Sample F-12 before failure (five cycles). (b) Sample F-12 during failure (five cycles). (c) Sample F-12 after failure (five cycles). (d) Sample F-21 before failure (ten cycles). (e) Sample F-21 after failure (ten cycles).

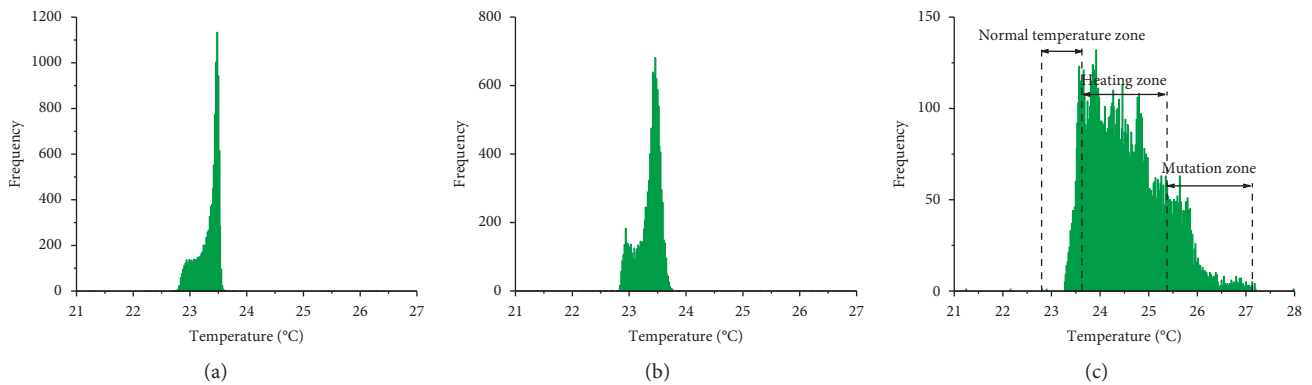


FIGURE 11: Frequency histogram under the 48% range of the unidirectional cyclic load, sample E-11. (a) Before destruction. (b) Under destruction. (c) After destruction.

Figures 11 and 12 reflect that the overall distribution of the regional temperature field is relatively uniform and that there is a central temperature before and during failure, but after failure, the temperature distribution area of the regional temperature field is apparently widened, and the uneven temperature distribution inside the sample can be revealed. The temperature field distribution area after destruction can be divided into three areas, namely, the normal temperature area, the heating area, and the mutation area. The normal temperature area can be determined by the ambient temperature, the area with a temperature higher than that of the normal temperature area is the heating area, and the last one is the mutation area. The area is a high-temperature area, but the frequency is low, which is caused by the high-temperature area

formed by stress concentration. Moreover, there are fewer high-temperature zones, that is, the stress concentration zones are more limited. Therefore, the concentration degree and range ratio of the stress concentration area can be evaluated. Furthermore, the larger the temperature range of the temperature distribution field is after the sample is destroyed, the more the heat exchange with the environment, and the lower the final detection temperature. The test results show that at a range of 60%, the detection temperature is lower, showing a wider area of the temperature field distribution after failure. In the 48% range, the width of the temperature field after failure is narrow, and the detection temperature is slightly higher. The results of infrared detection are closely related to the damage morphology and structure.

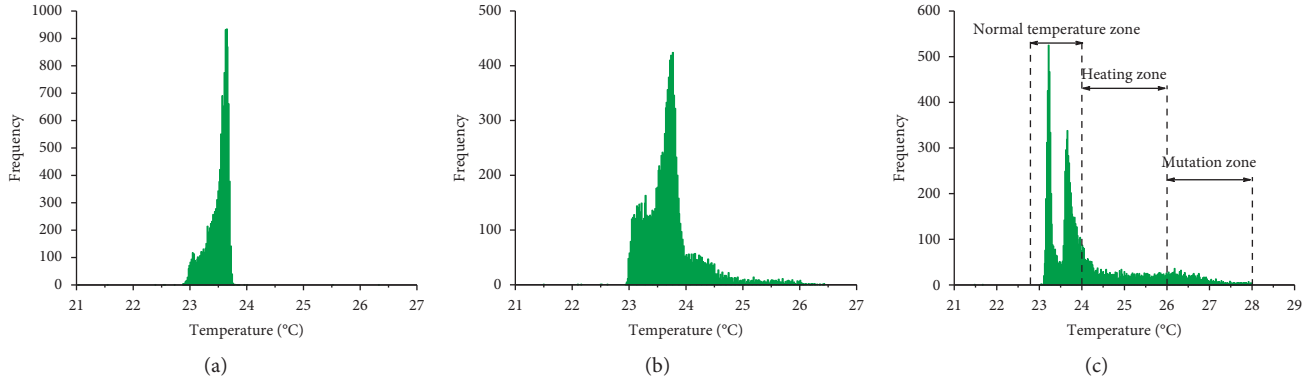


FIGURE 12: Frequency histogram under the 60% range of the unidirectional cyclic load, sample F-21. (a) Before destruction. (b) Under destruction. (c) After destruction.

The frequency histogram after failure reflects the temperature nonuniformity. It can better reveal and measure the energy distribution, measure the degree of stress concentration, and determine the location of the stress concentration area. It is also clear that when the rock sample is destroyed, it has undergone a process of normal temperature-heating-cooling thermal energy, which shows that there is a process of energy accumulation that is released in the process of pressure failure of the rock sample. In addition, the frequency histogram provides a superior evaluation platform, which can effectively realize the evaluation of the corresponding high-temperature area distribution and high-temperature range and has a positive effect on the analysis of the energy concentration and release law of the rock in the failure process.

**3.3. Loading and Unloading Effects of the Rock Mass considering Energy Release.** The cyclic loading and unloading process is the process of external force exerting work on the rock, including various energy conversions. Specifically, the total external force input  $U_i$  is converted into recoverable elastic strain energy  $U_i^e$ , plastic potential energy  $U_i^p$ , and surface energy formed between cracks and cracks after loading and unloading  $U_i^s$ , the radiant energy  $U_i^M$ , and kinetic energy  $U_i^v$  released at the time of destruction, as well as other unknown energies  $U_i^x$ . These energies are cross-coupled, and as a result, only a conceptual coupling expression equation can be established, that is,  $U_i = f(U_i^e + U_i^p + U_i^s + U_i^M + U_i^v + U_i^x)$ . It is difficult to solve this equation. Combined with the theory of energy conservation and related scholars, the action of external force  $U_i$  can be summarized as releasable elastic strain energy  $U_i^e$  and dissipated energy  $U_i^d$ . This principle is shown in Figure 13.

$$U_i = U_i^d + U_i^e. \quad (1)$$

The energy analysis reveals that the external force will increase the dissipated energy of the rock mass, and a part of the dissipated energy will form an energy accumulation, which will affect the thermal energy in the energy conversion. Each cycle of loading and unloading will form a certain

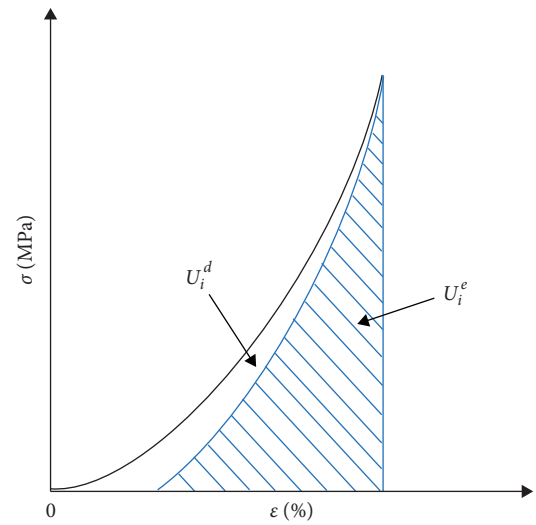


FIGURE 13: Schematic diagram of the compression energy of rock.

amount of energy accumulation, but at the same time, it will cause damage such as crack expansion. When the limit is not exceeded, the accumulated energy exerts an enhancement effect, leading to the final temperature increase. When the damage is more significant, it will cause greater energy dissipation, resulting in a decrease in temperature. In actual analysis, it is difficult to reflect the characteristics of the unloading damage of the rock mass if all the indicators such as the stress, strain, or plastic zone are used. The results of the infrared analysis clearly show that there is energy concentration and release in the process of loading and unloading failure of the rock. Naturally, the local energy release rate index can be introduced to improve it.

When damage occurs in the substance or irreversible changes occur in the damage, energy changes will inevitably occur in the substance. When the rock is damaged, a significant local temperature rise occurs. Therefore, the constitutive model needed in the loading and unloading calculations can be discussed and determined from irreversible thermodynamic theory [46, 47].

In continuum mechanics, if you want to start from thermodynamics, the constitutive equation must first satisfy

the Clausius–Duhamel inequality [48]. Assuming that the deformation process is infinitely small in temperature, the Clausius–Duhamel inequality can be expressed as

$$\sigma_{ij}\dot{\varepsilon}_{ij} - \dot{\varphi} \geq 0. \quad (2)$$

In the formula,  $\sigma_{ij}$  and  $\dot{\varepsilon}_{ij}$  are the stress and infinitesimal strain tensors, respectively, and  $\dot{\varphi}$  is the Helmholtz free energy density function.

Since the rock material is brittle and has significant anisotropy, a single scalar damage variable  $D$  can be defined by a meso set, which can be expressed by a double scalar and  $D$  as the internal variable, that is,

$$\varphi = \varphi(\varepsilon_{ij}, D). \quad (3)$$

The processes of loading and unloading of the rock mass are time-related; thus, the following equation can be obtained after the time derivative of equation (3):

$$\dot{\varphi} = \frac{\partial \varphi}{\partial \varepsilon_{ij}} \dot{\varepsilon}_{ij} + \frac{\partial \varphi}{\partial D} \dot{D}. \quad (4)$$

Equation (5) can be obtained after substituting formula (4) into formula (2):

$$\sigma_{ij} = \frac{\partial \varphi}{\partial \varepsilon_{ij}} \dot{\varepsilon}_{ij} - \frac{\partial \varphi}{\partial D} \dot{D} \geq 0. \quad (5)$$

If inequality (5) is to be true for any value, it should meet the following condition:

$$\sigma_{ij} = \frac{\partial \varphi}{\partial \varepsilon_{ij}}. \quad (6)$$

The free energy release rate  $Y$  can be defined as

$$Y = \frac{\partial \varphi}{\partial D}, \quad (7)$$

where  $Y$  is the dual generalized force of the damage variable  $D$ .

According to equations (6) and (7), inequality (5) can be rewritten as

$$Y\dot{D} \geq 0, \quad (8)$$

where  $YD$  is the damage dissipated power during damage.

If it is assumed that the internal damage process of the rock is irreversible, then the following must be true:

$$\begin{aligned} D &\geq 0, \\ \dot{D} &\geq 0, \\ Y &\geq 0. \end{aligned} \quad (9)$$

According to irreversible thermodynamics, it can be assumed that there is a dissipation potential  $\varphi^*$ . Taking the dual variables of  $\varepsilon_{ij}$  and  $D$  as internal variables, which are  $\sigma_{ij}$  and  $Y$ , the damage evolution equation can be derived according to the orthogonal flow law of internal variables:

$$\dot{D} = \frac{\partial \varphi^*}{\partial Y}. \quad (10)$$

In summary, according to the theory of irreversible thermodynamics, the damaged material has a strain energy density  $\varphi$  and a dissipation potential  $\varphi^*$ , through which the damage-strain coupling constitutive equation, the damage-strain energy release rate equation, and the general form of the damage evolution equation can all be derived.

To further consider the influence of strain, the general form of the strain-damage constitutive equation and damage-strain energy release rate equation can be derived according to equations (6) and (7).

Assuming that in the initial state, that is, the state before the force is initiated,  $Y=D=0$  and  $\sigma_{ij} = \varepsilon_{ij} = 0$ , then the Helmholtz free energy density  $\varphi$  can be expressed by the Taylor series as follows [49]:

$$\varphi(\varepsilon_{ij}, D) = \varphi_0 + \sum_{n=1}^N C^{(n)} D^n + \sum_{n=0}^N B_{ij}^{(n)} \varepsilon_{ij} D^n + \frac{1}{2} \sum_{n=0}^N A_{ijkl}^{(n)} \varepsilon_{ij} \varepsilon_{kl} D^n. \quad (11)$$

In the formula,  $\varphi_0$  is the free energy of the rock in the initial state, which can be 0;  $C^{(n)}$  is the scalar value coefficient; and  $A_{ijkl}^{(n)}$  and  $B_{ij}^{(n)}$  are the fourth- and second-order tensor coefficients.

Substituting formula (11) into formulas (6) and (7), the following equations can be obtained:

$$\sigma_{ij} = \sum_{n=0}^N B_{ij}^{(n)} D^n + \frac{1}{2} \sum_{n=0}^N A_{ijkl}^{(n)} \varepsilon_{kl} D^n, \quad (12)$$

$$Y = \sum_{n=1}^N C^{(n)} n D^{n-1} - \sum_{n=1}^N B_{ij}^{(n)} \varepsilon_{ij} n D^{n-1} - \frac{1}{2} \sum_{n=1}^N A_{ijkl}^{(n)} \varepsilon_{ij} \varepsilon_{kl} n D^{n-1}. \quad (13)$$

For rock loading and unloading, the rock mass has to undergo a loading process first and then be completely unloaded. In this process, the damage is irreversible. Hence,  $\sigma_{ij} = \varepsilon_{ij} = 0$ ,  $Y=0$ , and  $D \neq 0$ , where  $D$  could be any positive value, then

$$\begin{aligned} B_{ij}^{(n)} &= 0, \\ C^{(n)} &= 0 \quad (n \text{ could be any value}). \end{aligned} \quad (14)$$

Equations (12) and (13) can be simplified as

$$\sigma_{ij} = \sum_{n=0}^N A_{ijkl}^{(n)} \varepsilon_{kl} D^n, \quad (15)$$

$$Y = -\frac{1}{2} \sum_{n=1}^N A_{ijkl}^{(n)} \varepsilon_{ij} \varepsilon_{kl} n D^{n-1}. \quad (16)$$

Setting  $D=0$  and assuming  $A_{ijkl}^{(0)} = C_{ijkl}$ , equations (12) and (16) can be changed to

$$\begin{aligned} \varphi(\varepsilon_{ij}) &= \frac{1}{2} C_{ijkl} \varepsilon_{ij} \varepsilon_{kl}, \\ \varepsilon_{ij} &= C_{ijkl} \varepsilon_{ij} \varepsilon_{kl}. \end{aligned} \quad (17)$$

During the damage process, the internal porosity of the rock changes more uniformly, then

$$\begin{aligned} C_{ijkl} &= \lambda \delta_{ij} \delta_{kl} + \mu (\delta_{ik} \delta_{jl} + \delta_{il} \delta_{jk}), \\ A_{ijkl}^{(n)} &= -\lambda \alpha^n \delta_{ij} \delta_{kl} - \mu (\delta_{ik} \delta_{jl} + \delta_{il} \delta_{jk}). \end{aligned} \quad (18)$$

Finally, the stress-strain constitutive equation and damage-strain energy release rate equation of rock can be expressed as

$$\begin{aligned} \sigma_{ij} &= 2\mu \varepsilon_{ij} \left( 1 - \sum_{n=1}^N \beta^{(n)} D^n \right) + \lambda \varepsilon_{kk} \delta_{ij} \left( 1 - \sum_{n=1}^N \alpha^{(n)} D^n \right), \\ Y &= \frac{1}{2} \lambda \sum_{n=1}^N \alpha^{(n)} n D^{n-1} (\varepsilon_{kk})^2 + \mu \sum_{n=1}^N \beta^{(n)} n D^{n-1} \varepsilon_{ij} \varepsilon_{ij}. \end{aligned} \quad (19)$$

Local energy release indicators can be introduced to facilitate the output of energy-related parameters in the mechanical analysis of rock mass loading and unloading [50, 51]. In underground mining projects, no goaf is formed by excavation at one time, and there will not be only one stope. Therefore, during the service period of the mine, the loading and unloading process of the entire internal rock mass is ongoing. If it is assumed that the volume of the ore body under each excavation is  $dV$  and the energy released during each excavation is  $dW_r$ , then the energy release rate of each excavation can be defined as

$$ERR = \frac{dW_r}{dV}. \quad (20)$$

Considering that for a single stope, the blasting parameters of each excavation are relatively fixed, the energy release rate of each excavation is not much different. Therefore, the average energy release rate  $\overline{ERR}$  can be used in subsequent calculations after the formation of goafs:

$$\overline{ERR} = \frac{\sum_{i=1}^n ERR_i}{n}. \quad (21)$$

In the formula,  $n$  is the number of excavation cycles per stope.

Whether the phenomenon is due to the local temperature increase during the failure of the rock observed in the infrared test or obtained by the on-site engineering investigation, it can be found that the instability of the underground mine stope or empty area often starts from the local area because the elastic energy stored in the rock mass will suddenly be released locally when itself or its surroundings are under mining and disturbance. Obviously, this phenomenon of initial localized instability indicates that the average release rate can only describe the overall energy change law of the surrounding rock of the mine, but it cannot reflect the true process of instability of the surrounding rock. For this reason, it is necessary to further introduce the local energy release rate index to reflect this localized instability process. Therefore, the local energy release rate index is defined here, that is, the local energy release rate is the difference between the elastic energy

density before and after the failure of the rock mass element. This index can effectively characterize the change in strain energy before and after the failure of the surrounding rock. The index can be calculated by the following formula [52]:

$$LERR_i = ESED_{i_{max}} - ESED_{i_{min}}. \quad (22)$$

In the formula,  $LERR_i$  is the local energy release rate of rock unit  $i$ ;  $ESED_{i_{max}}$  is the maximum energy density of rock element  $i$  before failure; and  $ESED_{i_{min}}$  is the minimum energy density of rock element  $i$  before failure.

Therefore, the total energy released by all damaged units is the elastic release energy, which can be calculated by the following equation:

$$ERE = \sum_{i=1}^n (LERR_i V_i). \quad (23)$$

In the formula,  $V_i$  is the volume of the damaged rock unit  $i$ .

Consequently, the elastic strain energy density before and after element failure can be obtained as

$$\begin{aligned} ESED_{i_{max}} &= \frac{\sigma_1^2 + \sigma_2^2 + \sigma_3^2 - 2\mu(\sigma_1\sigma_2 + \sigma_1\sigma_3 + \sigma_2\sigma_3)}{2E}, \\ ESED_{i_{min}} &= \frac{\sigma_1'^2 + \sigma_2'^2 + \sigma_3'^2 - 2\mu(\sigma_1'\sigma_2' + \sigma_1'\sigma_3' + \sigma_2'\sigma_3')}{2E}. \end{aligned} \quad (24)$$

In the formula,  $\sigma_1$ ,  $\sigma_2$ , and  $\sigma_3$  refer to the corresponding principal stress before the failure of the rock element, while  $\sigma_1'$ ,  $\sigma_2'$ , and  $\sigma_3'$  represent that, after the failure of the rock element,  $\mu$  is the Poisson's ratio and  $E$  is the elastic modulus.

In summary, the local energy release index can better reflect the complex energy release of surrounding rock under different stress states, and the energy release, transfer, and dissipation law of the rock mass during the loading and unloading process can be effectively considered [40].

## 4. Conclusions

On the basis of summarizing the current conventional analysis methods and combining the research results for the mechanical characteristics and damage laws of the loading and unloading of rock, the loading and unloading mechanism of underground mining is analyzed. Through the infrared test on the rock uniaxial compression process after loading and unloading cycles, the energy release rate index is introduced to construct the loading and unloading analysis model of underground geotechnical engineering disturbance.

- (1) Cyclic loading and unloading will affect the infrared results of granite compression. When the damage is limited, the infrared radiation temperature increases. If the damage exceeds a certain limit, cyclic loading and unloading will reduce the infrared radiation temperature. When the granite is damaged, there will be a sharp increase in local temperature caused by the local stress concentration, as well as conspicuous

temperature fluctuations before and after the failure. In the meantime, the rock will release a large amount of heat at the moment of failure, and the temperature will rise sharply. Through the frequency histogram, the temperature field after failure can be divided into three temperature zones, that is, the normal temperature zone, heating zone, and mutation temperature zone, which comprehensively reflects that the compression failure of the rock is accompanied by energy accumulation and release.

- (2) A damage constitutive model that can consider energy evolution is selected and derived, and the local energy release rate indicator for rock mass engineering is introduced to reconstruct the loading and unloading mechanical analysis model of underground engineering excavation, considering energy release. The program can reflect the complex energy release of the surrounding rock under different stress states. The laws of energy release, transfer, and dissipation of the rock mass during the loading and unloading process are also taken into consideration, which can provide an effective basis for the restoration analysis of engineering problems and disaster warnings.

## Data Availability

Most of the data supporting this study are included in this article, and all of the data are available from the corresponding author on reasonable request.

## Conflicts of Interest

The authors declare that they have no conflicts of interest.

## Acknowledgments

The authors gratefully acknowledge the support from the National Natural Science Foundation of China (no. 51774323); the Natural Science Foundation of Hunan Province, China (no. 2020JJ4704); and the Fundamental Research Funds for the Central Universities of Central South University, China (Grant no. 2018zzts216). The corresponding author is grateful for the financial support of China Scholarship Council.

## References

- [1] R. Singh, A. S. Venkatesh, T. H. Syed et al., "Stable isotope systematics and geochemical signatures constraining groundwater hydraulics in the mining environment of the Korba Coalfield, Central India," *Environmental Earth Sciences*, vol. 77, no. 548, 2018.
- [2] F. Triscritti, "Mining, development and corporate-community conflicts in Peru," *Community Development Journal*, vol. 48, no. 3, pp. 437–450, 2013.
- [3] A. Li, F. Dai, Y. Liu, H. B. Du, and R. C. Jiang, "Dynamic stability evaluation of underground cavern sidewalls against flexural toppling considering excavation-induced damage," *Tunnelling and Underground Space Technology*, vol. 112, Article ID 103903, 2021.
- [4] B. Li, R. Bao, Y. Wang, R. Liu, and C. Zhao, "Permeability evolution of two-dimensional fracture networks during shear under constant normal stiffness boundary conditions," *Rock Mechanics and Rock Engineering*, vol. 54, no. 1, pp. 409–428, 2021.
- [5] Z. Tao, C. Zhu, M. He, and M. Karakus, "A physical modeling-based study on the control mechanisms of negative Poisson's ratio anchor cable on the stratified toppling deformation of anti-inclined slopes," *International Journal of Rock Mechanics and Mining Sciences*, vol. 138, Article ID 104632, 2021.
- [6] Q.-X. Meng, W.-Y. Xu, H.-L. Wang, X.-Y. Zhuang, W.-C. Xie, and T. Rabczuk, "DigiSim — an open source software package for heterogeneous material modeling based on digital image processing," *Advances in Engineering Software*, vol. 148, Article ID 102836, 2020.
- [7] H. Huang, T. Babadagli, X. Chen, H. Li, and Y. Zhang, "Performance comparison of novel chemical agents for mitigating water-blocking problem in tight gas sandstones," *SPE Reservoir Evaluation & Engineering*, vol. 23, no. 4, pp. 1150–1158, 2020.
- [8] Q. Wang, H. Gao, B. Jiang, S. Li, M. He, and Q. Qin, "In-situ test and bolt-grouting design evaluation method of underground engineering based on digital drilling," *International Journal of Rock Mechanics and Mining Sciences*, vol. 138, Article ID 104575, 2021.
- [9] J. Qiu, Z. Guo, L. Yang, H. Jiang, and Y. Zhao, "Effects of packing density and water film thickness on the fluidity behaviour of cemented paste backfill," *Powder Technology*, vol. 359, pp. 27–35, 2020.
- [10] Y. Wang, G. Zheng, and X. Wang, "Development and application of a goaf-safety monitoring system using multi-sensor information fusion," *Tunnelling and Underground Space Technology*, vol. 94, Article ID 103112, 2019.
- [11] Q. Wang, Q. Qin, B. Jiang et al., "Mechanized construction of fabricated arches for large-diameter tunnels," *Automation in Construction*, vol. 124, Article ID 103583, 2021.
- [12] Y. Wang, B. Zhang, S. H. Gao, and C. H. Li, "Investigation on the effect of freeze-thaw on fracture mode classification in marble subjected to multi-level cyclic loads," *Theoretical and Applied Fracture Mechanics*, vol. 111, Article ID 102847, 2021.
- [13] H. Huang, T. Babadagli, H. Li, K. Develi, and D. Zhou, "A visual experimental study on proppants transport in rough vertical fractures," *International Journal of Rock Mechanics and Mining Sciences*, vol. 134, p. 104446, 2020.
- [14] C. Zhu, M. He, M. Karakus, X. Zhang, and Z. Tao, "Numerical simulations of the failure process of anaclinal slope physical model and control mechanism of negative Poisson's ratio cable," *Bulletin of Engineering Geology and the Environment*, vol. 80, no. 4, pp. 3365–3380, 2021.
- [15] B. D. Snartland and C. Thaulow, "Fracture toughness testing at the micro-scale-The effect of the unloading compliance method," *Engineering Fracture Mechanics*, vol. 235, Article ID 107135, 2020.
- [16] S. Wang, W. Xu, L. Yan, X. Feng, W. Xie, and H. Chen, "Experimental investigation and failure mechanism analysis for dacite under true triaxial unloading conditions," *Engineering Geology*, vol. 264, Article ID 105407, 2020.
- [17] R. Shen, T. Chen, T. Li et al., "Study on the effect of the lower limit of cyclic stress on the mechanical properties and acoustic emission of sandstone under cyclic loading and unloading," *Theoretical and Applied Fracture Mechanics*, vol. 108102661 pages, 2020.

- [18] D. N. Dewhurst and A. L. Hennig, "Geomechanical properties related to top seal leakage in the Carnarvon Basin, Northwest Shelf, Australia," *Petroleum Geoscience*, vol. 9, no. 3, pp. 255–263, 2003.
- [19] H. Lewis, P. Olden, and G. D. Couples, "Geomechanical simulations of top seal integrity," *Hydrocarbon Seal Quantification: Norwegian Petroleum Society Special Publication*, vol. 11, pp. 75–87, 2002.
- [20] C. Hermanrud, H. M. N. Bols, and G. M. G. Teige, "Seal failure related to basin-scale processes," *The American Association of Petroleum Geologists Hedberg Series*, vol. 2, pp. 13–22, 2005.
- [21] G. M. G. Teige, C. Hermanrud, O. S. Kløvjan, P. Emil Eliassen, H. Løseth, and M. Gading, "Evaluation of caprock integrity in the western (high-pressured) haltenbanken area - a case history based on analyses of seismic signatures in overburden rocks," *Norwegian Petroleum Society Special Publications*, vol. 11, pp. 233–242, 2002.
- [22] K. Ogata, K. Senger, A. Braathen, and J. Tveranger, "Fracture corridors as seal-bypass systems in siliciclastic reservoir-cap rock successions: field-based insights from the Jurassic Entrada Formation (SE Utah, USA)," *Journal of Structural Geology*, vol. 66, pp. 162–187, 2014.
- [23] R. Cao, R. Yao, J. Meng, Q. Lin, H. Lin, and S. Li, "Failure mechanism of non-persistent jointed rock-like specimens under uniaxial loading: laboratory testing," *International Journal of Rock Mechanics and Mining Sciences*, vol. 132, Article ID 104341, 2020.
- [24] R. Cao, C. Wang, R. Yao et al., "Effects of cyclic freeze-thaw treatments on the fracture characteristics of sandstone under different fracture modes: laboratory testing," *Theoretical and Applied Fracture Mechanics*, vol. 109, Article ID 102738, 2020.
- [25] G. M. Ingram and J. L. Urai, "Top-seal leakage through faults and fractures: the role of mudrock properties," *Geological Society, London, Special Publications*, vol. 158, no. 1, pp. 125–135, 1999.
- [26] T. Wen, H. Tang, J. Ma, and Y. Liu, "Energy analysis of the deformation and failure process of sandstone and damage constitutive model," *KSCE Journal of Civil Engineering*, vol. 23, no. 2, pp. 513–524, 2019.
- [27] Z. M. He, Z. F. Liu, X.-H. Liu, and H.-B. Bian, "Improved method for determining active earth pressure considering arching effect and actual slip surface," *Journal of Central South University*, vol. 27, no. 7, pp. 2032–2042, 2020.
- [28] Z.-M. He, D. Xiang, Y.-X. Liu, Q.-F. Gao, and H.-B. Bian, "Deformation behavior of coarse-grained soil as an embankment filler under cyclic loading," *Advances in Civil Engineering*, vol. 2020, p. 4629105, 2020.
- [29] Y. Bazaikin, B. Gurevich, S. Iglauer et al., "Effect of CT image size and resolution on the accuracy of rock property estimates," *Journal of Geophysical Research: Solid Earth*, vol. 122, no. 5, pp. 3635–3647, 2017.
- [30] B. Chen, J. Xiang, J. P. Latham, and R. R. Bakker, "Grain-scale failure mechanism of porous sandstone: an experimental and numerical FDEM study of the Brazilian Tensile Strength test using CT-Scan microstructure," *International Journal of Rock Mechanics and Mining Sciences*, vol. 132, Article ID 104348, 2020.
- [31] Z. Pan, K. Zhou, R. Gao, Z. Jiang, C. Yang, and F. Gao, "Research on the pore evolution of sandstone in cold regions under freeze-thaw weathering cycles based on NMR," *Geofluids*, vol. 2020, Article ID 8849444, 2020.
- [32] R. Gao, K. Zhou, W. Liu, and Q. Ren, "Correlation between the pore structure and water retention of cemented paste backfill using centrifugal and nuclear magnetic resonance methods," *Minerals*, vol. 10, no. 7, 2020.
- [33] J. Gallwey, M. Eyre, and J. Coggan, "A machine learning approach for the detection of supporting rock bolts from laser scan data in an underground mine," *Tunnelling and Underground Space Technology*, vol. 107, Article ID 103656, 2020.
- [34] Q. Lin, P. Cao, J. Meng, R. Cao, and Z. Zhao, "Strength and failure characteristics of jointed rock mass with double circular holes under uniaxial compression: insights from discrete element method modelling," *Theoretical and Applied Fracture Mechanics*, vol. 109, Article ID 102692, 2020.
- [35] R. Cao, R. Yao, T. Hu, C. Wang, K. Li, and J. Meng, "Failure and mechanical behavior of transversely isotropic rock under compression-shear tests: laboratory testing and numerical simulation," *Engineering Fracture Mechanics*, vol. 241, Article ID 107389, 2020.
- [36] L. L. Rasmussen, P. P. Cacciari, M. M. Futai, M. M. de Assis, and A. P. Assis, "Efficient 3D probabilistic stability analysis of rock tunnels using a Lattice Model and cloud computing," *Tunnelling and Underground Space Technology*, vol. 85, pp. 282–293, 2019.
- [37] C. Yang, K. Zhou, R. Gao, and X. Xiong, "Numerical investigation of the dynamic response of a preconditioned roof in an underground mine: a case study of mining environment regeneration," *Soil Dynamics and Earthquake Engineering*, vol. 140, Article ID 106457, 2021.
- [38] C. Yang, K. Zhou, Z. Li, X. Xiong, Y. Lin, and Z. Luo, "Numerical modeling on the fracturing and energy evolution of large deep underground openings subjected to dynamic disturbance," *Energies*, vol. 13, p. 2020.
- [39] C. Yang, K. Zhou, X. Xiong, H. Deng, and Z. Pan, "Experimental investigation on rock mechanical properties and infrared radiation characteristics with freeze-thaw cycle treatment," *Cold Regions Science and Technology*, vol. 183, Article ID 103232, 2021.
- [40] B. Pan and K. Li, "A fast digital image correlation method for deformation measurement," *Optics and Lasers in Engineering*, vol. 49, no. 7, pp. 841–847, 2011.
- [41] Y. Xu, W. Yao, S. Wang, and K. Xia, "Investigation of the heat-treatment effect on rock fragmentation characteristics using the dynamic ball compression test," *Rock Mechanics and Rock Engineering*, vol. 53, no. 5, pp. 2095–2108, 2020.
- [42] S. Mineo and G. Pappalardo, "The use of infrared thermography for porosity assessment of intact rock," *Rock Mechanics and Rock Engineering*, vol. 49, no. 8, pp. 3027–3039, 2016.
- [43] H. Sun, L. Ma, N. Adeleke, and Y. Zhang, "Background thermal noise correction methodology for average infrared radiation temperature of coal under uniaxial loading," *Infrared Physics & Technology*, vol. 81, pp. 157–165, 2017.
- [44] H. Sun, X. L. Liu, S. G. Zhang, and K. Nawnit, "Experimental investigation of acoustic emission and infrared radiation thermography of dynamic fracturing process of hard-rock pillar in extremely steep and thick coal seams," *Engineering Fracture Mechanics*, vol. 226, Article ID 106845, 2020.
- [45] R. Shen, H. Li, E. Wang et al., "Infrared radiation characteristics and fracture precursor information extraction of loaded sandstone samples with varying moisture contents," *International Journal of Rock Mechanics and Mining Sciences*, vol. 130, Article ID 104344, 2020.
- [46] R. Shan, Y. Bai, Y. Ju, T. Han, H. Dou, and Z. Li, "Study on the triaxial unloading creep mechanical properties and damage constitutive model of red sandstone containing a single ice-

- filled flaw,” *Rock Mechanics and Rock Engineering*, vol. 54, pp. 1–23, 2021.
- [47] X. S. Liu, J. G. Ning, Y. L. Tan, and Q. H. Gu, “Damage constitutive model based on energy dissipation for intact rock subjected to cyclic loading,” *International Journal of Rock Mechanics and Mining Sciences*, vol. 85, pp. 27–32, 2016.
- [48] L. Huang and I. Dražić, “Large-time behavior of solutions to the 3-D flow of a compressible viscous micropolar fluid with cylindrical symmetry,” *Mathematical Methods in the Applied Sciences*, vol. 41, no. 17, pp. 7888–7905, 2018.
- [49] P. Korotaev, M. Belov, and A. Yanilkin, “Reproducibility of vibrational free energy by different methods,” *Computational Materials Science*, vol. 150, pp. 47–53, 2018.
- [50] S. Zhu, Y. Feng, F. Jiang, and J. Liu, “Mechanism and risk assessment of overall-instability-induced rockbursts in deep island longwall panels,” *International Journal of Rock Mechanics and Mining Sciences*, vol. 106, pp. 342–349, 2018.
- [51] F. Gao, H. Kang, J. Lou, J. Li, and X. Wang, “Evolution of local mine stiffness with mining process: insight from physical and numerical modeling,” *Rock Mechanics and Rock Engineering*, vol. 52, no. 10, pp. 3947–3958, 2019.
- [52] Y. Fan, J. Zheng, X. . Hu, X. Cui, and W. He, “Study on energy release of surrounding rock under the multiple unloading disturbance during tunnel excavation,” *Mathematical Problems in Engineering*, vol. 2020, Article ID 6486815, , 2020.